JOURNAL OF SYNCHROTRON RADIATION

ISSN 1600-5775

Received 30 December 2020
Accepted 30 March 2021

Edited by Y. Amemiya, University of Tokyo, Japan

Keywords: partially coherent light; mutual optical intensity; extreme ultraviolet interference lithography; beamlines.

Analysis of partially coherent light propagation through the soft X-ray interference lithography beamline at SSRF

Xiangyu Meng,[a] Huaina Yu,[a] Yong Wang,[a,b]* Junchao Ren,[b] Chaofan Xue,[a] Shuimin Yang,[a] Zhi Guo,[a,b] Jun Zhao,[a]* Yanqing Wu[a,b]* and Renzhong Tai[a,b]

[a]Shanghai Advanced Research Institute, Chinese Academy of Sciences, 239 Zhangheng Road, Pudong District, Shanghai 201800, People's Republic of China, and [b]Shanghai Institute of Applied Physics, Chinese Academy of Sciences, 239 Zhangheng Road, Pudong District, Shanghai 201800, People's Republic of China.
*Correspondence e-mail: wangyong@zjlab.org.cn, zhaojun@zjlab.org.cn, wuyanqing@zjlab.org.cn

The mutual optical intensity (MOI) model is extended to the simulation of the interference pattern produced by extreme ultraviolet lithography with partially coherent light. The partially coherent X-ray propagation through the BL08U1B beamline at Shanghai Synchrotron Radiation Facility is analysed using the MOI model and *SRW* (*Synchrotron Radiation Workshop*) method. The fringe intensity at the exposure area is not uniform but has similar envelope lines to Fresnel diffraction, which is explained by the diffraction from the finite grating modelled as a single aperture. By balancing the slit size and photon stop size, the fringe visibility, photon flux and intensity slope can be optimized. Further analysis shows that the effect of pink light on the aerial images is negligible, whereas the third-harmonic light should be considered to obtain a balance between high fringe visibility and high flux. Two grating interference exposure experiments were performed in the BL08U1B beamline. The aerial image depth showed that the polymethyl methacrylate photoresist depth was determined by the X-ray coherence properties.

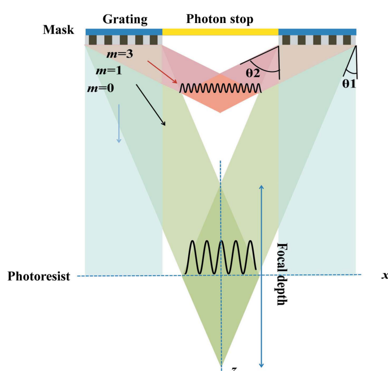

1. Introduction

Extreme ultraviolet interference lithography (EUV-IL) is currently considered the leading technology to manufacture future generations of semiconductor devices (Päivänranta *et al.*, 2011). EUV-IL is based on the use of interference transmission gratings at a wavelength of 13.5 nm, which enables the manufacture of high-volume patterns with sub-10 nm feature sizes (Fan & Ekinci, 2016). EUV-IL is also a powerful tool for EUV photoresist evaluation under working conditions. Since no manufacturer can tolerate the risk of potential contamination of the equipment by the novel photoresist on the expensive commercial EUV lithography machine, the EUV-IL technique is currently considered the only feasible EUV photoresist evaluation tool (Lio, 2016). EUV-IL requires coherent illumination to produce periodic patterns (Solak *et al.*, 2003). However, the beam provided by third-generation synchrotron radiation sources is not fully but partially coherent. The partial coherence decreases the pattern contrast and resolution (Solak *et al.*, 2002). Therefore, it is necessary to accurately analyse the effect of coherence properties on EUV-IL for the EUV photoresist evaluation and manufacture of high-quality patterns.

Packages have been developed to simulate partial coherent light propagation through synchrotron beamlines. The *SRW* (*Synchrotron Radiation Workshop*) code (Chubar *et al.*, 2011) calculates the spontaneous emission of electrons from the

synchrotron insertion device and simulates the wavefront propagation through beamlines based on the Fourier optics approach. The *HYBRID* code (Shi *et al.*, 2014) can analyse the partially coherent light propagation by combining ray tracing and wavefront propagation. *XRT* (*X-Ray Tracer*) is a python software library for ray tracing and wave propagation in the X-ray regime. In wave propagation, partially coherent radiation is treated as incoherent addition of coherently diffracted fields generated per electron (Klementiev & Chernikov, 2014). Recently, the mutual optical intensity (MOI) model has been developed to analyse the spatially partial coherent X-ray propagation through mirrors and reflecting gratings (Meng *et al.*, 2015, 2017). The MOI model can directly simulate the propagation of the entire mutual optical intensity through the beamline, which contains the full coherence information of the wavefront. By extending the MOI model to the EUV-IL setup, we can analyse the effect of the partial coherence on the periodic patterns.

In this paper, the partially coherent light propagation through the BL08U1B beamline at the Shanghai Synchrotron Radiation Facility (SSRF) is calculated using the MOI model and *SRW* package. We adopt the MOI model to simulate the interference of two partially coherent beams that pass through the transmission gratings and project the intensity profile onto the exposure area. The fringe visibility, photon flux and intensity slope at the exposure area are optimized by changing the slit and photon stop sizes. Furthermore, the effects of pink light and third-harmonic light on EUV-IL are analysed. The two-grating interference exposure experiment was performed in the BL08U1B beamline. The polymethyl methacrylate (PMMA) photoresist depth with various slit sizes was obtained using atomic force microscopy (AFM).

2. Theory and modelling

Fig. 1 illustrates the general scheme of EUV-IL; two coherent beams are diffracted by a grating of period q through angle θ for diffraction order m, which generates a standing wave pattern that can be projected as an aerial image onto the exposure area (Jang *et al.*, 2007; Mojarad *et al.*, 2015). The intensity profile for the fringe pattern is given by (Saidani & Solak, 2009; Buitrago *et al.*, 2016)

$$I = 4I_0 \sin^2(\pi x/p), \tag{1}$$

$$p = \frac{\lambda}{2\sin\theta} = \frac{q}{2m}, \tag{2}$$

where I_0 is a constant representing the maximum intensity, p is the period of the interference pattern in the x direction and λ is the beam wavelength. Equation (1) can be used to roughly describe the interference patterns generated at the exposure area. However, the synchrotron radiation is partially coherent X-rays, which can reduce the fringe visibility. In addition, the intensity and phase at the exposure area are not uniformly distributed. Therefore, it is necessary to analyse the effect of synchrotron radiation on the interference pattern. In this paper, we extend the MOI model to calculate the partially coherent light propagation through EUV-IL.

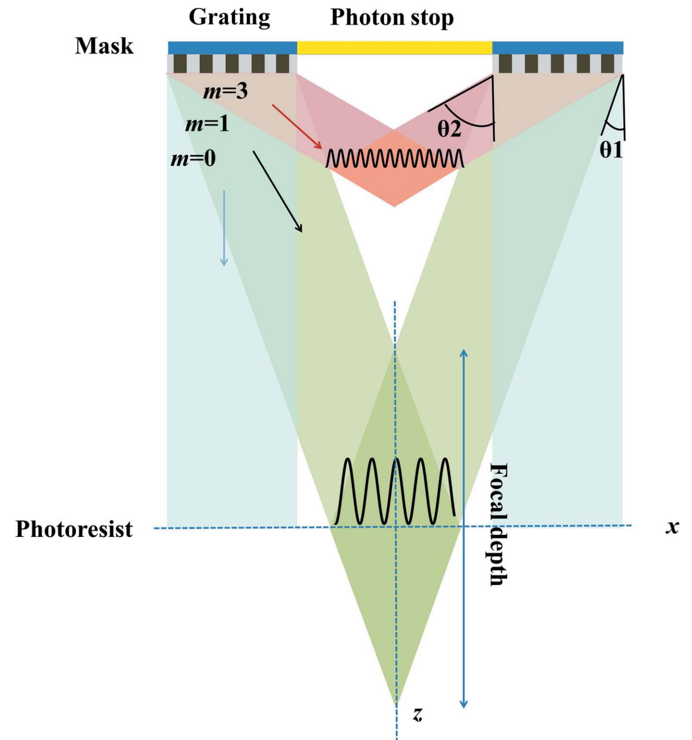

Figure 1
Schematic of the interference lithography.

The MOI model uses the mutual optical intensity to describe the coherence properties. The four-dimensional mutual optical intensity $J(P_1, P_2)$ provides the electric field distribution and correlation between any two points P_1 and P_2. The intensity at point P_1 can be expressed by $J(P_1, P_1)$. The propagation of the mutual optical intensity from the source plane $J(P_1, P_2)$ to the image plane $J(Q_1, Q_2)$ through free space is represented by the following equation (Mandel & Wolf, 1995; Goodman, 2015),

$$J(Q_1, Q_2) = \iint\iint J(P_1, P_2)\exp\left[-i\frac{2\pi}{\lambda}(r_2 - r_1)\right] \times \frac{\chi(\theta_1)}{\lambda r_1}\frac{\chi(\theta_2)}{\lambda r_2}\,\mathrm{d}S_1\,\mathrm{d}S_2, \tag{3}$$

where λ is the wavelength; r_1 and r_2 are the P_1-to-Q_1 and P_2-to-Q_2 distances; $\chi(\theta_1)$ and $\chi(\theta_2)$ are the inclination factors for inclination angles θ_1 and θ_2; S_1 and S_2 are the surfaces of the source.

The MOI model is extended to address light transmission through a grating. The basic optical setup for EUV-IL is shown in Fig. 1. Two partially coherent beams pass through two linear diffraction gratings, followed by the projection of the resulting interference patterns onto the exposure area. The MOI model calculation for EUV-IL [based on equation (3)] can be performed in three steps. First, each grating period is represented as one element; the beam is assumed to have constant complex amplitude and full coherence in one period at the grating plane. This assumption is valid because the

grating period is much smaller than the beam size and transverse coherence length. The amplitude transmission function for one period can be expressed as $T(P) = \exp(i2\pi/\lambda nt)$, where t and n are the grating thickness and refractive index, respectively. Thus, the mutual optical intensity at the exit plane of the grating can be expressed as $J(\tilde{P}_1, \tilde{P}_2) = T(P_2^* J(P_1, P_2) T(P_1)$. Second, the propagation for each element in the MOI model is calculated using the Fraunhofer or Fresnel approximation (Born & Wolf, 1999). Finally, the mutual optical intensity at the exposure area is realized by summing the contributions of all elements,

$$J(Q_1, Q_2) = \sum_{mn} \left[A^*_{mnQ_2} \sum_{jk} J(P_{jk}, P_{mn}) A_{jkQ_1} \right], \qquad (4)$$

where j, k, m and n are the element indexes at the grating plane;

$$A_{jkQ_1} = \iint \exp\left(i \frac{2\pi}{\lambda} r_{P_{jk}Q_1} \right) \frac{\chi(\theta_1)}{\lambda r_{P_{jk}Q_1}} T\left(P_{jk}\right) \mathrm{d}S_{jk}. \qquad (5)$$

3. Spatial coherence simulation

3.1. Beamline layout

The BL08U beamline at the SSRF has two branches: BL08U1A for the scanning transmission X-ray microscopy (STXM) and BL08U1B for EUV-XIL. An elliptically polarized undulator (EPU) with a length of 4.2 m and a period of 100 mm is used to generate high-brilliance and partially coherent X-rays. The source provides the energy range 85–150 eV by changing the EPU gap. The EUV-XIL beamline layout is shown in Fig. 2. A four-blade aperture (aperture stop) is located 20 m downstream from the EPU source, which can block undesirable photons and define the acceptance angle for the beamline. The first cylindrical mirror (CM1) and secondary cylindrical mirror (CM2) are located at 22 m and 22.9 m to horizontally and vertically focus the beam at the exit slit (slit) plane at 26 m, respectively. Two branches can be alternated by switching the CM1 mirror with a grazing incident angle of 1.5°. The CM2 mirror has a larger grazing incident angle for the suppression of high-harmonic light. Both mirrors are vertically mounted to easily switch the beam between two branches and reduce the effect of gravity on the mirror surface. The slit size can be adjusted to balance the spatial coherence and photon flux at the endstation, which is located at 35 m.

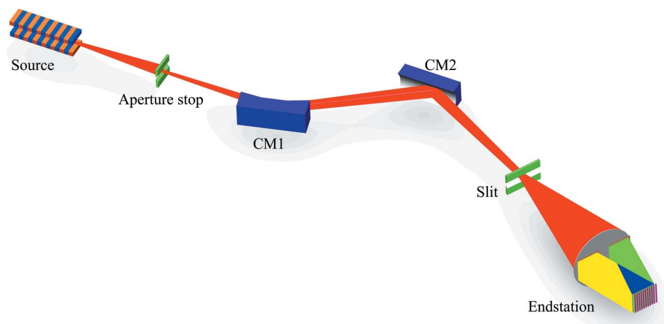

Figure 2
Optical layout of the BL08U1B beamline.

3.2. Partially coherent light propagation through the EUV-XIL beamline

In this section, the MOI and *SRW* models are used to simulate the partially coherent light propagation in the horizontal direction through the EUV-XIL beamline. At 92.5 eV, the source size σ and divergence angle σ' are 155 µm and 51.7 µrad, respectively, as obtained from *SPECTRA* (Tanaka & Kitamura, 2001). The source coherence length ξ (Vartanyants & Singer, 2010) of 41.6 µm is calculated from the following equation:

$$\frac{(2\pi\sigma')^2}{\lambda^2} = \frac{1}{4\sigma^2} + \frac{1}{\xi^2}. \qquad (6)$$

From the source size and coherence length, we can acquire a global degree of coherence of 0.13 (Vartanyants & Singer, 2010). When the aperture stop and slit sizes are 1100 µm and 90 µm, respectively, the intensity, coherence degree and cosine of wavefront profiles at the endstation are calculated as shown in Fig. 3. The MOI and *SRW* models have similar intensity profiles [*cf*. Fig. 3(*a*)]. The intensity full width at half-maximum (FWHM) at the endstation is 2085 µm. The coherence degree between any point and the central point is acquired using the MOI model, as shown in Fig. 3(*b*). Due to the finite acceptance of the aperture stop and slit, the global degree of coherence increases to 0.58, and the coherence length is 1146 µm by Gaussian fitting of the central coherence degree profile. Fig. 3(*c*) shows the distribution of the cosine of the phase within 2000 µm (FWHM). The plane wavefront is approximately 172 µm, which is much smaller than the spot size.

3.3. Intensity distribution through EUV-IL

The finite grating size can affect the wavefront propagation, leading to intensity oscillations near the edges of the pattern area (Lyndin *et al.*, 1997; Päivänranta *et al.*, 2011). It is necessary to accurately calculate the partially coherent X-ray propagation through EUV-IL masks. Since the *SRW* model cannot analyse X-ray propagation through EUV-IL, in this paper, we use the MOI model to calculate the effect of partially coherent light on EUV-IL. There are two amplitude Au gratings with 400 µm size, 280 nm period and 0.5 duty circle. The photon stop is 600 µm long, which acts to block the photons that do not directly pass through the gratings from reaching the photoresist and creating an exposure background. The aerial image is produced by first-order diffracted beams at 92.5 eV.

When the aperture stop and slit sizes are selected to be 1100 µm and 90 µm, the fringe intensity profile (black line) at the exposure area is shown in Fig. 4(*a*), which is composed of periodic features with large amplitudes. The optical intensity is not uniformly distributed in the exposure area, with a modulation profile similar to that expected from Fresnel diffraction.

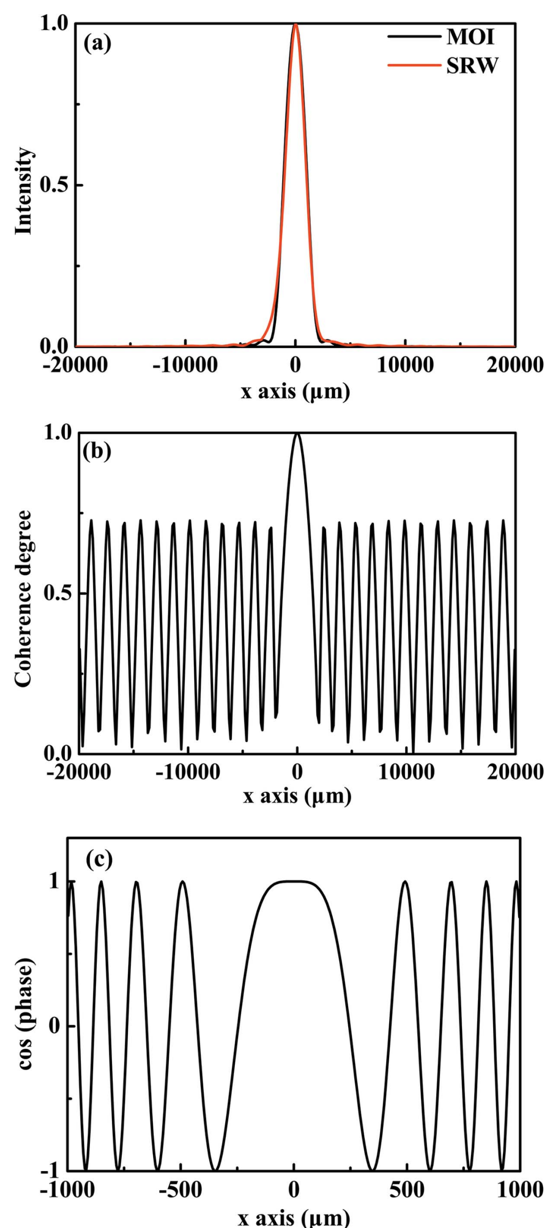

Figure 3
(*a*) Normalized intensity, (*b*) coherence degree and (*c*) cosine of phase profiles in the horizontal direction at the endstation. The coherence degree is defined between any point and the central point.

We can calculate the zeroth-order diffraction (red line) through the finite grating modelled as a single aperture, as shown in Fig. 4(*a*). The intensity profiles for the enlarged regions of 0–4 µm, 188–192 µm and 200–204 µm are shown in Figs. 4(*b*), 4(*c*) and 4(*d*), respectively. The intensity profile of the single-aperture diffraction is consistent with the intensity envelope line of the aerial image. Thus, the intensity envelope of the aerial image is defined by the projection of the zeroth-order diffraction of the finite grating as a single aperture onto the exposure area.

The intensity has a maximum at x = 190 µm. There are small-amplitude oscillations in the envelope line in the central region, which rapidly decrease when one moves towards the edge of the pattern. Despite the intensity oscillations, the aerial image period and fringe visibility remain constant at 140 nm and 0.67 ± 0.02 over the entire exposure area, respectively. In practical applications of EUV-IL, the gratings designed should be larger than the desired exposure area, so that any undesirable intensity variations near the edge areas can be excluded from the desired exposure area.

3.4. Optimization for EUV-IL

The exposure area is limited by the spatial coherence of the source, which can be improved by reducing the beam divergence angle at the cost of photon flux. The coherence can also be improved by reducing the photon stop size; however, a small photon stop increases the difficulties of the EUV-IL mask manufacture. The balance between coherence and photon flux is very important for high-quality interference patterns. In this section, the slit and photon stop sizes are optimized for uniform intensity at the grating plane and high photon flux and fringe visibility at the exposure area.

The intensity slope $s = (I_{\max} - I_{\min})/(I_{\max} + I_{\min})$ is used to roughly describe the intensity uniformity throughout the grating plane. Fig. 5(*a*) shows the intensity slope distribution at the grating plane with various slit and photon stop sizes. When the slit size is less than 50 µm, the intensity slope is approximately zero. Fig. 5(*b*) shows the normalized photon flux at the exposure area. The photon flux increase is more apparent when the slit size is increased than when the photon stop size is reduced. When the slit size is 50 µm, the photon flux is 0.35–0.42. Fig. 5(*c*) shows the fringe visibility at the exposure area. The fringe visibility can be improved by reducing the slit size or photon stop size. When the slit size is less than 50 µm, the fringe visibility is almost 1 even if the photon stop size is very large. Fig. 5 shows that the uniform intensity, photon flux and fringe visibility can be optimized by changing the slit size and photon stop size.

3.5. Chromatic light

In practical applications of EUV-IL, the illuminating light is not monochromatic and has finite bandwidth and high harmonics. We analysed the intensity and fringe visibility with pink light taking beamline BL08U1B as an example. The energy bandwidth of the pink light is 3.2 eV at 92.5 eV. The pink light is evenly separated into 30 monochromatic lights from 85 eV to 100 eV with the intensity distribution according to the *SPECTRA* results (Tanaka & Kitamura, 2001). The aperture stop and slit sizes are 1100 µm and 80 µm, respectively. The interference pattern for every monochromatic light is calculated using the MOI model and summed with intensity to obtain the entire pattern for the pink light. The fringe visibility for chromatic light is 0.76, approximately 1.3% less than that for monochromatic light. The small decrease comes from the difference in the intensity envelope profile in the interference pattern for different monochromatic light. This indicates that the finite bandwidth has no effect on the aerial image and that the EUV-IL system is robust for temporal coherence.

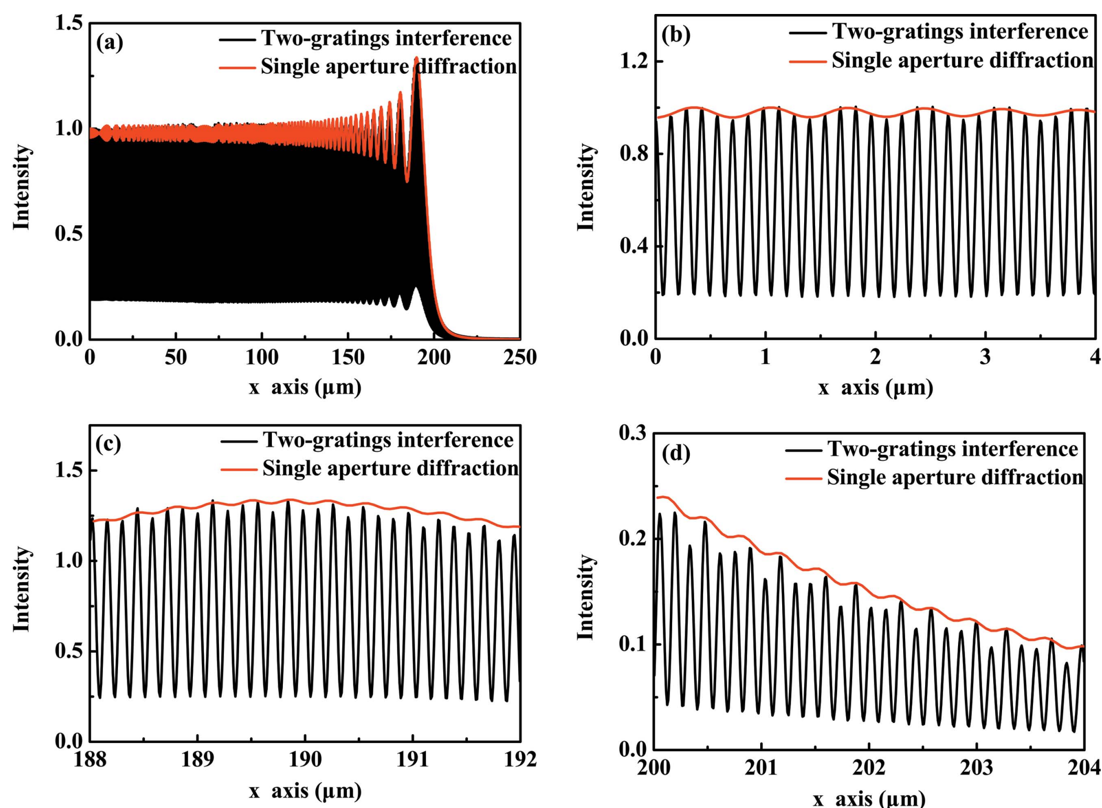

Figure 4
(*a*) Normalized intensity profiles in the *x* direction calculated using the MOI model. Intensity profiles in the enlarged regions (*b*) 0–4 μm, (*c*) 188–192 μm and (*d*) 200–204 μm. The black lines denote the results obtained for the EUV-IL, and the red lines denote the results obtained from Fresnel diffraction for a single aperture.

The third-harmonic light (277.5 eV) has a 7.6% flux of the fundamental light at the endstation. It is necessary to analyse the effect of high harmonics on the EUV-IL. The optical schematic diagram of the illuminations from different diffraction orders is shown in Fig. 6(*a*). The first- and third-order diffractions of the third-harmonic light have cross sections with the exposure area of the first-order diffraction of the fundamental light. The first-order diffraction efficiency of the third-harmonic light is comparable to that of the fundamental light and should be considered in the total interference pattern. The total pattern on the exposure area is acquired by adding the intensity profiles of the fundamental and third-harmonic lights. Fig. 6(*b*) shows the total intensity distribution at the exposure area generated by the fundamental light and third-harmonic light, and the inset shows the intensity profile generated only by the third-harmonic light. The inset also shows that the contribution of the first-order diffraction of the third-harmonic light covers the right half of the intensity profile, while that of the third-order diffraction is small. Compared with the intensity profile without harmonic light [*cf.* Fig. 2(*a*)], the intensity profile with harmonic light increases slightly in the right half of the range. Therefore, in the left half, the fringe visibility remains unchanged, while in the right half, the fringe visibility decreases from 0.76 to 0.71 due to the third-harmonic light. The high harmonics can be suppressed by increasing the grazing angle of the harmonics suppression mirror but at the cost of the photon flux. The balance between photon flux and fringe visibility should be

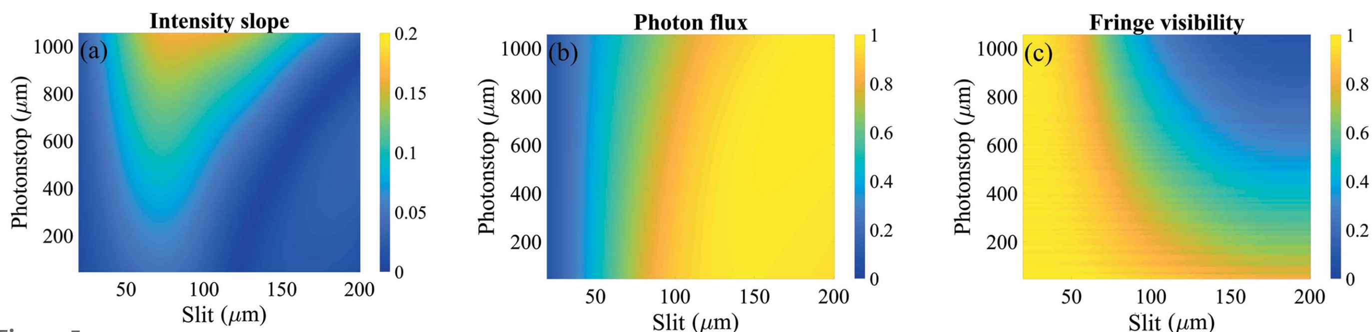

Figure 5
(*a*) Intensity slope distribution at the grating plane, (*b*) normalized photon flux and (*c*) fringe visibility distribution at the exposure area.

optimized to obtain the best quality pattern. By varying the grazing angle of the harmonics suppression mirror from 0.5° to 15°, we obtain the fringe visibility and flux in Fig. 6(*c*). The normalized flux at the grating decreases from 0.98 to 0.5 when increasing the grazing angle. Both fringe visibilities in the two regions increase when the grazing angle increases but with different trends. The fringe visibility slowly increases from 0.71 to 0.76 in the region when the *x* axis is small, yet it increases dramatically from 0.31 to 0.76 in the illuminating area of the first diffraction of the third-harmonic light. The third-harmonic light has an apparent effect on the fringe visibility in almost half of the exposure area of the fundamental light. The grazing angle of the harmonics suppression mirror should be optimized to achieve a balance between flux and fringe visibility.

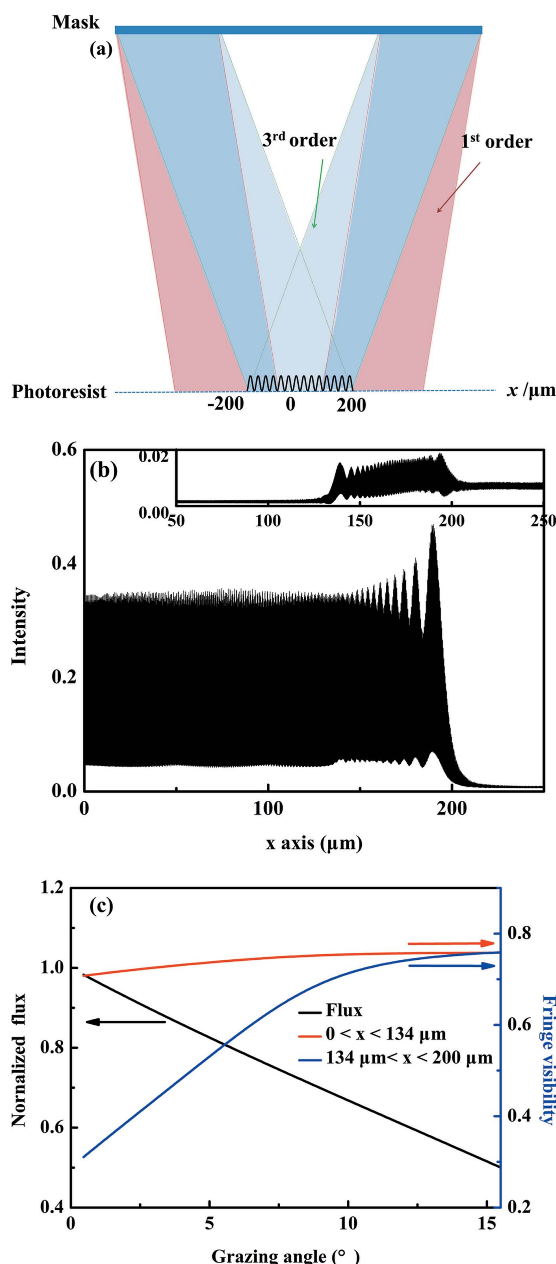

Figure 6
(*a*) Schematic diagram of the third-harmonic light propagation through gratings. (*b*) Intensity distribution at the exposure area generated by the fundamental light and third-harmonic light. The inset shows the intensity profile generated by the third-harmonic light. (*c*) Normalized flux and fringe visibility as a function of the grazing angle.

4. Experimental

Two grating interference exposure experiments were performed in the horizontal direction in the BL08U1B beamline. The EUV-IL mask used transmission gratings with a 280 nm period and 0.5 duty circle. The square grating and photon stop were both 400 μm. PMMA is commonly used as a high-resolution positive resist for EUV microlithographic processes. First, PMMA (Micro-Chem PMMA A2, 950k) was spin-coated on a silicon wafer, which resulted in a photoresist thickness of 70 nm. Then, it was baked for 1.5 min at 180°C. EUV-IL exposures were performed with aperture stop size of 900 μm, and the exposure dose was approximately 555 mJ cm^{-2} with an energy of 92.5 eV. The photoresist was located at the exposure area to record the fringe intensity distribution through the EUV-IL mask. After the exposure, the samples were developed in MIBK diluted 1:3 in IPA for 45 s, rinsed with alcohol for 30 s and dried by a gentle N_2 flow. Finally, aerial images with a 140 nm period were obtained.

A beam position monitor (BPM) was located 4.6 m downstream from the slit and could be used to measure the coherence property at the endstation. The BPM consisted of two carbon wires. Photoelectrons could be recorded when X-rays reached the wires. The intensity profiles were obtained by scanning the BPM within the range from −5 mm to 5 mm with steps of 0.03 mm. The experimental results detected by the BPM and theoretical results calculated by the MOI model are shown in Fig. 7(*a*). For slit sizes of 40–80 μm, the experimental and theoretical results coincided with each other. The global degree of coherence at the endstation was 0.93, 0.84, 0.75 and 0.67 for slit sizes of 40 μm, 60 μm, 80 μm and 100 μm, respectively (see Table 1). The PMMA film depth before exposure was 67 nm, as measured using an AST SE200-BM spectroscopic ellipsometer. The PMMA depth of aerial images after the exposure was measured using AFM. When the slit sizes were 40 μm, 60 μm, 80 μm and 100 μm, the PMMA depths were 64.2 nm, 63.5 nm, 61.4 nm and 57.7 nm, respectively. The normalized PMMA depth (red markers) with various slit sizes is shown in Fig. 7(*b*). With increasing slit size, the global degree of coherence decreased on the two-grating mask. The low global degree of coherence decreased the fringe visibility and destroyed the PMMA depth at the exposure area. In addition, the MOI model was used to simulate the fringe intensity distribution at the exposure area. The intensity ratio $(I_{\max} - I_{\min})/I_{\max}$ (black markers) was calculated as shown in Fig. 7(*b*), where $I_{\max}$ and $I_{\min}$ were the maximum and minimum of the fringe intensity profile, respectively. The normalized PMMA depth and intensity ratio with various slit sizes were similar. When the slit size was 40 μm, we used AFM to obtain the PMMA aerial image, as shown in Fig. 7(*c*). The aerial image showed a line structure with a 140 nm period and 64.2 nm depth. Fig. 7 indicates that

Table 1
Global degree of coherence and PMMA thickness with different slit sizes.

	Slit size (μm)			
	40	60	80	100
Global degree of coherence	0.93	0.84	0.75	0.67
PMMA thickness (nm)	64.2	63.5	61.4	57.7

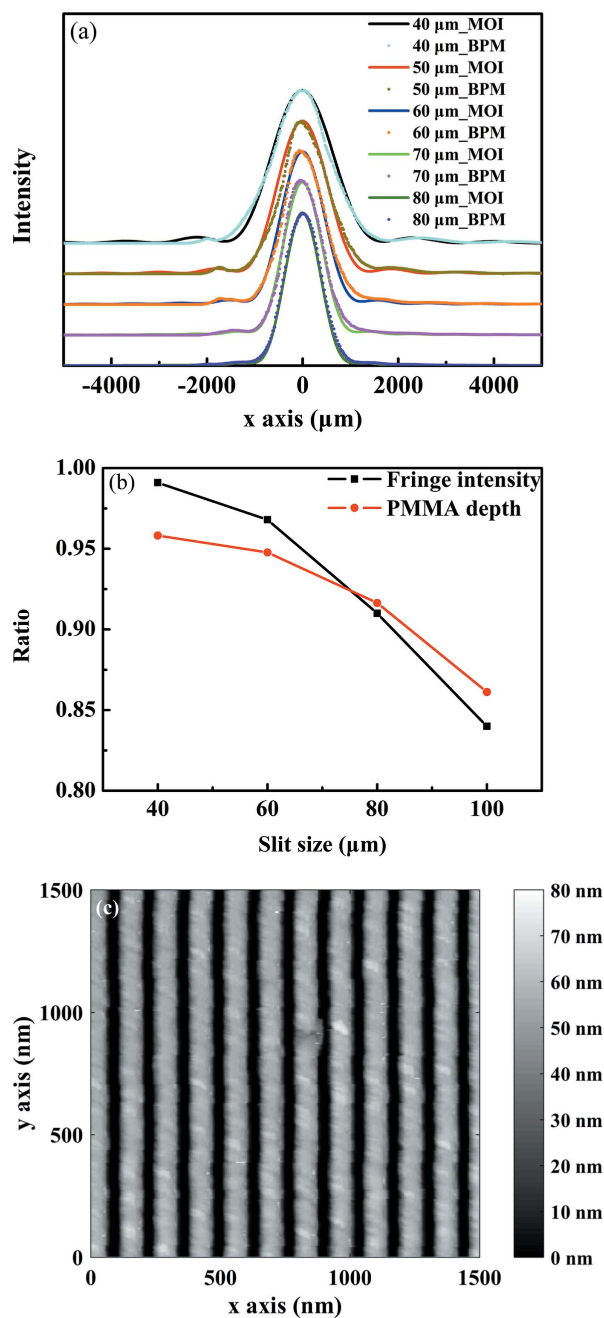

Figure 7
(*a*) Intensity profiles at the BPM position with various slit sizes. The curves are theoretical results from the MOI model, and the dots are experimental results from the BPM scanning in the horizontal direction. (*b*) Intensity ratio (black markers) from the MOI model and normalized PMMA depth (red markers) from AFM with various slit sizes. (*c*) PMMA aerial image with a 140 nm period.

the PMMA depth was determined by the X-ray coherence. The difference between PMMA depth and intensity ratio might come from other factors, such as the transmission rate and vibrational effect. By optimizing the slit size, the photon flux and fringe visibility could be balanced to obtain high-quality PMMA nanostructures, which is important for nano-device fabrication and EUV photoresist testing.

5. Conclusions

The MOI model is developed to analyse EUV-IL with partially coherent light by considering the phase shift and amplitude attenuation induced by the diffraction grating. The aerial image intensity through the two-grating mask is non-uniform in the exposure area, which is due to Fresnel diffraction from the finite grating modelled as a single aperture. Despite the intensity oscillations, the aerial image period and fringe visibility remain unchanged over the entire exposure area. To improve the quality of aerial images, the intensity slope, photon flux and fringe visibility are optimized by changing the slit and photon stop sizes. Further analysis shows that the effect of pink light on aerial images is negligible; however, the contribution of the third-harmonic light is relatively large, and the harmonic suppression mirror should be optimized to balance the flux and fringe visibility. Two grating interference exposure experiments were performed in the BL08U1B beamline at SSRF. With a slit size of 40 μm, the PMMA depth was 64.2 nm and satisfied the demand of high-quality aerial images. The EUV-IL experiments show that the PMMA depth is determined by the X-ray coherence. The MOI model can calculate the partially coherent X-ray propagation through beamlines and obtain the intensity distribution through a two-grating mask. These advantages make the MOI model a useful tool for the optimization of EUV-IL.

Funding information

This work was supported by the National Natural Science Foundation of China (Nos. 11875314, U1632268, 11705272, U1832110 and U1832104), the Ministry of Science and Technology of China (grant No. 2017YFA0403400), the National Key Basic Research Program of the China Science and Technology Commission of Shanghai Municipality (grant No. 17JC1400802) and the National Key Research and Development Program (grant No. 2016YFB0700402).

References

Born, M. & Wolf, E. (1999). *Principles of Optics*. Cambridge University Press.

Buitrago, E., Fallica, R., Fan, D., Kulmala, T. S., Vockenhuber, M. & Ekinci, Y. (2016). *Microelectron. Eng.* **155**, 44–49.

Chubar, O., Berman, L., Chu, Y. S., Fluerasu, A., Hulbert, S., Idir, M., Kaznatcheev, K., Shapiro, D., Shen, Q. & Baltser, J. (2011). *Proc. SPIE*, **8141**, 814107.

Fan, D. & Ekinci, Y. (2016). *J. Micro-Nanolith.* **15**, 033505.

Goodman, J. W. (2015). *Statistical Optics*. New York: John Wiley.

Jang, J. H., Ullal, C. K., Maldovan, M., Gorishnyy, T., Kooi, S., Koh, C. Y. & Thomas, E. L. (2007). *Adv. Funct. Mater.* **17**, 3027–3041.

Klementiev, K. & Chernikov, R. (2014). *Proc. SPIE*, **9209**, 92090A.

Lio, A. (2016). *Proc. SPIE*, **9776**, 97760V.
Lyndin, N., Parriaux, O. & Sychugov, V. (1997). *Sens. Actuators B Chem.* **41**, 23–29.
Mandel, L. & Wolf, E. (1995). *Optical Coherence and Quantum Optics*. Cambridge University Press.
Meng, X., Shi, X., Wang, Y., Reininger, R., Assoufid, L. & Tai, R. (2017). *J. Synchrotron Rad.* **24**, 954–962.
Meng, X. Y., Xue, C. F., Yu, H. N., Wang, Y., Wu, Y. Q. & Tai, R. Z. (2015). *Opt. Express*, **23**, 29675–29686.
Mojarad, N., Gobrecht, J. & Ekinci, Y. (2015). *Microelectron. Eng.* **143**, 55–63.
Päivänranta, B., Langner, A., Kirk, E., David, C. & Ekinci, Y. (2011). *Nanotechnology*, **22**, 375302–375308.
Saidani, M. & Solak, H. H. (2009). *Microelectron. Eng.* **86**, 483–485.
Shi, X., Reininger, R., Sanchez del Rio, M. & Assoufid, L. (2014). *J. Synchrotron Rad.* **21**, 669–678.
Solak, H. H., David, C., Gobrecht, J., Golovkina, V., Cerrina, F., Kim, S. O. & Nealey, P. F. (2003). *Microelectron. Eng.* **67–68**, 56–62.
Solak, H. H., David, C., Gobrecht, J., Wang, L. & Cerrina, F. (2002). *Microelectron. Eng.* **61–62**, 77–82.
Tanaka, T. & Kitamura, H. (2001). *J. Synchrotron Rad.* **8**, 1221–1228.
Vartanyants, I. A. & Singer, A. (2010). *New J. Phys.* **12**, 035004.